Ultrasound in Med. & Biol., Vol. 37, No. 3, pp. 345–357, 2011

0301-5629/$ - see front matter

doi:10.1016/j.ultrasmedbio.2010.11.020

● *Original Contribution*

THREE-DIMENSIONAL HIGH-FREQUENCY BACKSCATTER AND ENVELOPE QUANTIFICATION OF CANCEROUS HUMAN LYMPH NODES

Jonathan Mamou,* Alain Coron,[†‡] Michael L. Oelze,[§] Emi Saegusa-Beecroft,[¶] Masaki Hata,[¶] Paul Lee,* Junji Machi,[¶] Eugene Yanagihara,[¶] Pascal Laugier,[†‡] and Ernest J. Feleppa*

*F. L. Lizzi Center for Biomedical Engineering, Riverside Research Institute, New York, NY; [†]UPMC Univ Paris 06, UMR 7623, LIP, Paris, France; [‡]CNRS, UMR 7623 Laboratoire d'Imagerie Paramétrique, Paris, France; [§]Bioacoustics Research Laboratory, Department of Electrical and Computer Engineering, University of Illinois, Urbana, IL; and [¶]University of Hawaii and Kuakini Medical Center, Honolulu, HI

(*Received* 20 *April* 2010; *revised* 5 *October* 2010; *in final form* 22 *November* 2010)

Abstract—Quantitative imaging methods using high-frequency ultrasound (HFU) offer a means of characterizing biological tissue at the microscopic level. Previously, high-frequency, 3-D quantitative ultrasound (QUS) methods were developed to characterize 46 freshly-dissected lymph nodes of colorectal-cancer patients. 3-D ultrasound radiofrequency data were acquired using a 25.6-MHz center-frequency transducer and each node was inked before tissue fixation to recover orientation after sectioning for 3-D histological evaluation. Backscattered echo signals were processed using 3-D cylindrical regions-of-interest (ROIs) to yield four QUS estimates associated with tissue microstructure (*i.e.*, effective scatterer size, acoustic concentration, intercept and slope). These QUS estimates, obtained by parameterizing the backscatter spectrum, showed great potential for cancer detection. In the present study, these QUS methods were applied to 112 lymph nodes from 77 colorectal and gastric cancer patients. Novel QUS methods parameterizing the envelope statistics of the ROIs using Nakagami and homodyned-K distributions were also developed; they yielded four additional QUS estimates. The ability of these eight QUS estimates to classify lymph nodes and detect cancer was evaluated using receiver operating characteristics (ROC) curves. An area under the ROC curve of 0.996 with specificity and sensitivity of 95% were obtained by combining effective scatterer size and one envelope parameter based on the homodyned-K distribution. Therefore, these advanced 3-D QUS methods potentially can be valuable for detecting small metastatic foci in dissected lymph nodes. (E-mail: jmamou@riversideresearch.org) © 2011 World Federation for Ultrasound in Medicine & Biology.

Key Words: **High-frequency ultrasound, Quantitative ultrasound, Lymph nodes, Micrometastases, Cancer.**

INTRODUCTION

High-frequency (*i.e.*, >15 MHz) ultrasound (HFU) permits investigating biological tissue at microscopic levels with spatial resolutions on the order of 100 μm. Recent successful HFU studies have permitted imaging shallow or low-attenuation tissues for biomedical applications. For instance, HFU already has been successfully used for small animal (Turnbull 2000; Turnbull and Foster 2002; Aristizábal et al. 1998; Mamou et al. 2009a), ocular (Silverman et al. 1995, 2008), intravascular (de Korte et al. 2000; Saijo et al. 2004) and dermatological imaging (Vogt and Ermert 2007; Huang et al. 2007).

Our group has demonstrated the ability of quantitative ultrasound (QUS) to characterize lymph node tissues from cancer patients (Mamou et al. 2010). Reliable determination of the presence or absence of metastatic cancer in lymph nodes is essential for staging disease and planning its treatment. Most human lymph nodes have sizes ranging from 2 to 10 mm in diameter and are sufficiently small to be imaged in their entirety in 3-D using HFU. The long-term objective of our lymph node studies is to develop QUS imaging methods that are capable of detecting small nodal metastases using echo-signal data from freshly-excised nodes for staging disease in patients who have known primary cancers in neighboring organs (*e.g.*, breast, colon, stomach). In routine pathology procedures, this method would direct the pathologist to suspicious regions that might be overlooked in conventional histology. In sentinel-node procedures, the method would serve as a basis for identifying sentinel nodes, detecting

Address correspondence to: Jonathan Mamou, F. L. Lizzi Center for Biomedical Engineering, Riverside Research Institute 156 William St., 9th floor, New York, NY 10038. E-mail: jmamou@riversideresearch.org

metastatic cancer and initiating formal (*i.e.*, complete) node dissections when sentinel nodes are positive for cancer. To achieve this long-term objective, QUS studies that were previously undertaken successfully (Mamou et al. 2010) have been improved, refined to include envelope statistics and applied to a larger number of lymph nodes.

This manuscript focuses on two different categories of QUS methods. The first category quantifies the backscattered spectrum deduced from the radiofrequency (RF) echo signals and the second category quantifies the statistics of the envelope-detected echo signals. The spectral methods were first established by Lizzi et al. (1983), and since this foundation work, many others (Insana et al. 1990; Feleppa et al. 1986; Oelze et al. 2002; Oelze and Zachary 2006; Mamou et al. 2008, 2010) have pushed this field forward and developed methods for tissue characterization and cell characterization (Kolios et al. 2002; Baddour et al. 2005). In these studies, the frequency-dependent backscattered information was used to assess tissue microstructural properties quantitatively and relate them to histological properties (Insana et al. 1990; Feleppa et al. 1986; Oelze et al. 2002). In particular, our group recently has shown promising results using backscatter-derived QUS estimates for the detection of metastases in freshly dissected lymph nodes from colorectal cancer patients (Mamou et al. 2010).

Many QUS studies have also been performed by modeling the envelope statistics for tissue characterization. These methods fit a specific distribution model to the observed distribution of the envelope-detected signals statistics. QUS estimates are obtained from the fit parameters and, similar to the QUS methods from backscatter quantification, the hypothesis is that these envelope-statistics–based QUS estimates provide a means of distinguishing between different tissue types. Many different distribution models (*e.g.*, Rayleigh, K, Nakagami) have been used for ultrasound tissue characterization (Wagner et al. 1987; Shankar et al. 2000, 2001; Shankar 2000). In a recent HFU study, the generalized gamma distribution showed promise at detecting structural changes during cell death in acute myeloid leukemia cells (Tunis et al. 2005).

In our studies, we decided to use the homodyned-K (HK) distribution. This distribution is more involved computationally, but it can model more complex ultrasound scattering situations (Dutt and Greenleaf 1994; Hao et al. 2002). All of the aforementioned distribution models, their relationships to one another, and their physical interpretation recently have been theoretically studied and described (Destrempes and Cloutier 2010); this study concluded that the HK distribution is the only model for which the distribution parameters retain a physical meaning in the case where the diffuse scattering vanishes. In addition, the HK distribution can model low scatterer densities correctly and also can quantify the coherent component in backscattered signals that originates from organized (subresolution) scatterers (Destrempes and Cloutier 2010). Because of its analytical complexity, the HK distribution model has been criticized (Shankar 2000; Eltoft 2005; Tsui and Chang 2007), and its use has been somewhat limited, whereas other, more analytically tractable models such as the Nakagami distribution (Shankar 2000; Tsui and Chang 2007), Weibull distribution (Raju and Srinivasan 2002), Rician inverse Gaussian distribution (Eltoft 2005) and the generalized gamma distribution (Raju and Srinivasan 2002) have been used. The HK distribution is defined by three independent parameters: (i) the μ parameter, which quantifies the number of scatterers per resolution cell; (ii) the s parameter, which quantifies the coherent signal; and (iii) the σ parameter, which quantifies the incoherent signal. A fourth parameter, the k parameter, is the ratio of the coherent to incoherent signal components. The richness of the parameterization improves interpretation of results when compared with estimates from other distributions, *e.g.*, the Nakagami distribution, which is a function of only two parameters. Nevertheless, in a recent study, the HK distribution was used in conjunction with computationally extensive algorithms to characterize cardiac tissues (Hao et al. 2002). More recently, a new parameter-estimation algorithm for the HK distribution was developed that is efficient and robust (Hruska et al. 2009; Hruska and Oelze 2009). This improved parameter-estimation algorithm provides more accurate information to better elucidate the relationships between the envelope statistics and the underlying structures responsible for the signals. In the present study, the ability of the HK distribution to quantify lymph node properties was assessed and fit parameters using the Nakagami distribution were also obtained for comparison. The Nakagami distribution had shown success in characterizing breast masses and was used here as a reasonable, high-quality reference (Shankar et al. 2001; Tsui et al. 2010).

The current standard histopathology procedure for lymph node evaluation has many limitations, and the possibility of detecting easily overlooked but clinically significant small metastases (particularly metastases that have a size between 0.2 and 2 mm) in excised lymph nodes using QUS approaches in quasi–real time could be valuable in mitigating these limitations. Currently, most lymph nodes dissected from a cancer patient are either sent to pathology for a thorough postoperative histological preparation and evaluation, or they first undergo a rapid intraoperative “touch-prep” procedure (*e.g.*, for sentinel nodes of breast cancer patients). Neither approach is able to detect all small metastases in lymph nodes, particularly micrometastases. Furthermore, the touch-prep approach produces a large number of false-negative determinations because the pathologist only examines cells exfoliated from two adjacent surfaces of the lymph node, and the cells derived from these surfaces may not reveal the presence of a small cancerous region within a metastatic node. In addition, a thorough histology preparation takes several days to produce results because several thin sections are evaluated by a pathologist, but it suffers fewer false-negative determinations.

The remainder of the present paper is organized into the following three sections: the Methods section briefly reviews our methods from surgery and lymph node preparation to QUS image formation and presents the new methods for characterization based on envelope statistics; the Results section presents results from the 112 lymph nodes studied to date; and finally, the Discussion section presents a detailed overview of the study to date and the next steps of the study.

METHODS

Surgery, lymph-node preparation and ultrasound data acquisition

The surgery, lymph node preparation and ultrasound data acquisition protocols for this study were identical to the previously described protocols (Mamou et al. 2010), and they are summarized next for completeness. Lymph nodes were dissected from patients with histologically proven primary cancers at the Kuakini Medical Center (KMC) in Honolulu, HI. The dissected nodes were prepared for pathology according to the current standard of care for surgical treatment of colorectal and stomach cancers. After surgical excision, dissected nodes were brought to the pathologist for gross preparation. Then, individual, manually-defatted lymph nodes were placed in a water bath containing isotonic saline (0.9% sodium chloride solution) at room temperature and ultrasonically scanned while pinned through a thin margin of fat to a piece of sound-absorbing material.

Ultrasound data were acquired with a focused, single-element transducer (PI30-2-R0.50IN, Olympus NDT, Waltham, MA, USA) that had an aperture of 6.1 mm and a focal length of 12.2 mm. The transducer had a center frequency of 25.6 MHz and a –6-dB bandwidth that extended from 16.4 to 33.6 MHz. The theoretically predicted axial and lateral resolutions of the HFU imaging system were 85 and 116 μm, respectively. The 6-dB depth of field was measured to be 1.6 mm extending from 11.4 to 13.0 mm. The transducer was excited by a Panametrics 5900 pulser/receiver unit (Olympus NDT), and the RF echo signals were digitized using an 8-bit Acqiris DB-105 A/D board (Acqiris, Monroe, NY, USA) at a sampling frequency of 400 MHz. The spacing between adjacent A-lines was 25 μm. A 3-D scan of each lymph node was obtained by scanning adjacent planes uniformly spaced every 25 μm over the entire lymph node. The RF data were oversampled to limit noise effects and to increase the robustness of some of the processing steps (*e.g.*, 3-D segmentation and attenuation compensation).

3-D backscatter and envelope characterization methods

Two different approaches were used to characterize and quantify the microstructural tissue properties of lymph nodes. The first approach was based on backscatter spectral quantification and the second approach modeled the envelope statistics of the backscattered signal. These two approaches were used to test the hypothesis that QUS estimates obtained from backscatter spectral and envelope quantification are statistically different between cancerous (*i.e.*, metastatic) and noncancerous tissue in lymph nodes. Subsequent sections in this paper describe in great detail the envelope statistics quantification, but they only briefly review the methods used for backscatter spectral quantification because they were previously published (Mamou et al. 2010).

3-D segmentation and cylindrical regions-of-interest

The 3-D RF datasets were segmented using a semi-automatic algorithm to separate nodal tissue from saline and remaining fibroadipose tissue. The segmentation algorithm has been presented and evaluated in great detail before and has not been modified significantly except for improvements in its computational efficiency (Coron et al. 2008; Mamou et al. 2010). After segmentation, the complete 3-D RF dataset was separated into overlapping 3-D cylindrical regions-of-interest (ROIs) with a diameter of 1 mm and a length (*i.e.*, along the axis of the transducer) of 1 mm. The size of the ROI was chosen based on the resolution cell of our imaging system. The overlap between adjacent ROIs depended on the total number of voxels of the 3-D RF dataset; it was adjusted to permit smaller datasets to have a sufficient number of ROIs for statistical stability and to avoid overly-long computation times for larger datasets (see Table 1 in Mamou et al. 2010).

Parameter estimation and QUS image formation

Estimates of spectral intercept (I in dB), spectral slope (S in dB/MHz), effective scatterer sizes (D in μm) and acoustic concentration (*i.e.*, CQ^2 expressed in dB mm^{-3}) were obtained using the previously published methods (Mamou et al. 2010). Briefly, these estimates were computed by fitting two different scattering models to normalized and attenuation-compensated ROI power spectra. Specifically, I and S were obtained by fitting a straight line to normalized power spectra, and D and

CQ^2 were obtained assuming a spherical Gaussian scattering model (Mamou et al. 2010). Attenuation compensation was performed independently for each ROI, assuming straight-line propagation from the transducer surface to the ROI. This attenuation-compensation approach took into account propagation through fat and lymph node tissue using two different attenuation values. The value for fat was estimated to be 0.97 dB/MHz/cm and the value for tissue was assumed to be 0.5 dB/MHz/cm; these values were assumed to be the same for every lymph node. Attenuation compensation previously was presented in great detail (Mamou et al. 2010).

In this study, four new QUS parameters were computed by fitting distribution models to the envelope statistics of each ROI. The first two parameters α and Ω were obtained using a maximum-likelihood estimator to fit a Nakagami probability density function (PDF) to that of the ROI envelope. The PDF of the Nakagami distribution is (Nakagami 1960):

$$f_{Nakagami}(r)=\frac{2\alpha^{\alpha}r^{2\alpha-1}}{\Gamma(\alpha)\Omega^{\alpha}}\exp\left(-\frac{\alpha}{\Omega}r^2\right)U(r), \qquad (1)$$

where Γ and U are the gamma function and unit step function, respectively. The parameter Ω is termed the *scaling parameter*, whereas α is usually called the *Nakagami parameter*. If R is a random variable with a Nakagami PDF, then

$$\Omega=E\left[R^2\right], \qquad (2)$$

and

$$\alpha=\frac{\left(E[R^2]\right)^2}{E\left[\left(R^2-E[R^2]\right)^2\right]}, \qquad (3)$$

where E is the expected value operator. The likelihood ratio was obtained by assuming that every envelope value within the ROI was independently and identically distributed. Then, the parameters α and Ω were found by maximizing the likelihood ratio using an ascent algorithm.

The Nakagami parameter, α, is a shape parameter for the PDF, and when it is equal to 1, the Nakagami distribution reduces to a Rayleigh distribution. In addition, when α is between 0 and 1, the envelope distribution is said to be pre-Rayleigh (Nakagami 1960). Finally, when $\alpha > 1$, the distribution is said to be post-Rayleigh (Shankar 2000). When the ROI contains randomly located scatterers with varying scattering cross sections, the envelope statistics are likely to be pre-Rayleigh and α is typically between 0.5 and 1 (Shankar 1995). Similarly, when some spatial periodicity exists among scatterers within the resolution cell, then the envelope statistics are Rician or post-Rayleigh, and α becomes larger than unity (Shankar 2000). Typically, α is used as a means to quantify the effective number of scatterers in the resolution cell. This interpretation can be obtained by noting that the random variable $Z = R^2$ follows a gamma distribution and interpreting the physical relationships between α and the effective number obtained from the gamma distribution (Shankar et al. 2001).

Two additional QUS parameters, k and μ, were obtained using the HK distribution to model the envelope statistics within the ROI. The HK distribution was first introduced in 1980 (Jakeman 1980). This distribution incorporates a capability to model situations with low or high scatterer densities, but also includes a capability to model situations where a coherent signal component exists because of periodically located scatterers (Dutt and Greenleaf 1994).

The PDF of the HK distribution is given by the following integral expression:

$$f_{HK}(r)=r\int_0^{+\infty} xJ_0(sx)J_0(rx)\left(1+\frac{x^2\sigma^2}{2\mu}\right)^{-\mu}\mathrm{d}x, \qquad (4)$$

where J_0 is the 0th-order Bessel function of the first kind, s^2 is the coherent signal energy, σ^2 is the diffuse signal energy and μ is a measure of the effective number of scatterers per resolution cell. A derived parameter, $k=s/\sigma$, the ratio of the coherent to the diffuse signal, can be used to describe the degree of structure or periodicity in scatterer locations. (No closed-form expression exists for f_{HK}, but a truncated converging series is used in practice [Hao et al. 2002].) We estimated k and μ for the HK distribution. Because of the complexity of eqn (4), no straightforward method exists to obtain these estimates. Methods using the first three even moments have been described, but were computationally expensive and could lead to complex estimates (Dutt and Greenleaf 1994). Instead, we used an algorithm that relied on moments of small orders (Hruska and Oelze 2009). For completeness, the algorithm is summarized below.

The new algorithm extended previous work (Martin-Fernandez et al. 2007) and estimated envelope statistics parameters by calculating the signal-to-noise ratio (SNR), skewness and kurtosis of fractional-order moments of the envelope samples in each ROI. The use of fractional-order moments was motivated by previous studies (Dutt and Greenleaf 1995; Ossant et al. 1998) that found that parameter estimates based on fractional-order moments were more robust than parameter estimates based on higher-order moments for the simpler, but related, K distribution. The optimal pair of fractional-order moments (*i.e.*, 0.72 and 0.88) to use in the estimation routine was determined by construction of level curves for SNR, skewness and kurtosis. The

SNR, skewness (Sk_ν) and kurtosis (Ku_ν) of samples of the echo envelope of moment ν can be expressed as (Prager et al. 2002; Hruska and Oelze 2009):

$$SNR_\nu = \frac{E[R^\nu]}{\left(E[R^{2\nu}] - E[R^\nu]^2\right)^{\frac{1}{2}}}, \tag{5}$$

$$Sk_\nu = \frac{E[R^{3\nu}] - 3E[R^\nu]E[R^{2\nu}] + 2E[R^\nu]^3}{\left(E[R^{2\nu}] - E[R^\nu]^2\right)^{\frac{3}{2}}}, \tag{6}$$

$$Ku_\nu = \frac{E[R^{4\nu}] - 4E[R^\nu]E[R^{3\nu}] + 6E[R^{2\nu}]E[R^\nu]^2 - 3E[R^\nu]^4}{\left(E[R^{2\nu}] - E[R^\nu]^2\right)^2}. \tag{7}$$

The optimal pair of fractional-order moments was found by calculating the maximal intersection angles between the six level curves generated at each pair of k and μ values over a range of values expected to be encountered in ultrasonic imaging (Hruska and Oelze 2009). For a given ROI size, using the optimal moment orders results in the smallest variance of envelope-parameter estimates over the range of possible parameter space expected for ultrasonic imaging. Assuming homogeneous scattering statistics in the ROI, larger ROIs result in smaller bias and variance in parameter estimates because the parameter estimates depend on acquiring a good statistical representation of the signal envelope. The sizes of the ROIs chosen for parameter estimation in this study were sufficiently large to ensure a good statistical representation of the underlying signal (Hruska 2009).

Using this approach, estimates of the k and μ parameters for each ROI were obtained in three steps. First, the envelope of the signal was detected and the values of the envelope corresponding to the ROI location were stored in a vector. Second, the SNR, skewness and kurtosis were calculated using eqns (5)–(7) for the vector of envelope values corresponding to the ROI using the chosen moment orders. Third, level curves previously generated and stored for the SNR, skewness and kurtosis corresponding to different values of the k and μ parameters for the two fractional-order moments (*i.e.*, 0.72 and 0.88) were used to find the intersection of the six level curves generated from the envelope values from the ROI in the $k-\mu$ plane.

The parameters μ and α were corrected to account for variations in the size of the resolution cell due to attenuation and diffraction effects. The correction algorithm multiplied the estimates by the term, κ, which varied for each ROI:

$$\kappa = \frac{B_{6dB}^{ROI}\left[f_c^{ROI}\right]^2}{B_{6dB} f_c^2}, \tag{8}$$

where f_c is the natural center frequency of the transducer (*i.e.*, 25.6 MHz in the present case), $B_{6dB}$is the –6-dB bandwidth of the transducer (*i.e.*, 33.6 – 16.4 = 17.2 MHz), and f_c^{ROI} and B_{6dB}^{ROI} are the same quantities, but estimated within the ROI by taking into account diffraction effects (using the calibration spectrum acquired at the depth corresponding to the ROI center) and attenuation effects (based on the sound path from the transducer to the ROI). Details about the calibration spectrum and attenuation estimation were previously presented (Mamou et al. 2010). The rationale behind eqn (8) is that the resolution cell of a single-element system is proportional to $\frac{1}{B_{6dB} f_c^2}$ (Kino 1987). Therefore, multiplying estimates of μ and α by κ permits comparison (and averaging) of these QUS estimates among different ROIs and different lymph nodes.

The parameter, Ω, is the only envelope-statistics parameter sensitive to the absolute range of the envelope values within the ROI. For example, multiplying the envelope values by a constant, δ, changes the value of Ω by a factor of δ^2, but does not change the values of α, k and μ. Therefore, Ω is the envelope parameter that is most sensitive to attenuation and diffraction effects. To mitigate the effects of attenuation and diffraction on Ω, envelope values for each ROI were multiplied by an ROI-dependent parameter, χ, which corrected for estimated attenuation and diffraction effects at 25.6 MHz, *i.e.*, at the center frequency of the transducer:

$$\chi = S_{oil}(f, z_{ROI})A(f), \text{ with } f = 25.6 \text{ MHz}, \tag{9}$$

where z_{ROI} is the depth at the center of the ROI, $S_{oil}(f, z_{ROI})$ is the calibration spectrum acquired at a depth equal to z_{ROI} and $A(f)$ is the attenuation-compensation function obtained for this ROI. The terms $A(f)$ and $S_{oil}(f, z_{ROI})$ are defined in eqns (1) and (5), respectively, in Mamou et al. (2010). Finally, because of their wide dynamic range, μ, α and Ω were compressed using a base-10 logarithm function.

These eight QUS parameters were estimated for all adjacent ROIs within the entire segmented lymph-node tissue. 3-D QUS images were formed by color-coding and overlaying the parameter values on the conventional B-mode volume. However, ROIs that were not fully contained in depths between z = 10.8 mm and z = 13.5 mm were not processed because they were judged to be too far away from the nominal focal depth of the transducer.

Materials used

The results described in the next section pertain to 112 lymph nodes excised from 77 different patients diagnosed with colorectal or gastric cancers. These lymph nodes either were entirely negative for metastases ($N = 92$), or were nearly completely filled with metastases ($N = 20$). The majority (*i.e.*, 98) of nodes were excised from colorectal cancer patients, but 14 nodes acquired from gastric cancer patients were also included in the study because of their availability. Although these lymph nodes were associated with cancers from different organs, they were grouped together for these studies because they present the same histopathologic features in healthy and diseased states (Mills 2006). Combining nodes of gastric with colorectal cancers is reasonable histologically because the basic architecture of non-neoplastic lymph nodes is similar among different organ systems in healthy and diseased states (van der Valk and Meijer 1987). Gastric and colorectal carcinomas are part of a diverse group of glandular epithelial neoplasms of the gastrointestinal tract that are composed of complex neoplastic glands in well- to moderately-differentiated lesions. Although subtle histologic differences may exist among them, these tumors generally present with the basic architecture of differentiated adenocarcinomas, *i.e.*, neoplastic gland formation. From this standpoint, colorectal and gastric carcinomas and their metastases are similar histologically. Metastatic lesions to lymph nodes tend to retain the histologic appearance of the primary cancer, which is uniform among primary adenocarcinomas of the gastrointestinal tract, *i.e.*, in gastric as well as colorectal cancers. Combining nodes in this manner is further justified by the results themselves, as presented in the next section. The nodes were diagnosed by a pathologist by examination of the hematoxylin and eosin (H&E)–stained sections.

The Institutional Review Boards (IRBs) of the University of Hawaii and the KMC approved the participation of human subjects in the study. All participants were recruited at KMC and gave written informed consent as required by both IRBs.

RESULTS

Illustrative parametric cross-section images and envelope PDFs

To illustrate the results of the 3-D QUS processing, Fig. 1 displays the three B-mode cross sections of an entirely non-metastatic lymph node; each B-mode image is augmented by the color-coded estimates of $\log(\mu)$. A color bar and histogram of the entire node distribution of $\log(\mu)$ are shown in Fig. 1d. The $\log(\mu)$ estimates show a fairly large distribution with a mean of –0.14 and a standard deviation of 0.22. For comparison, Fig. 2 displays the $\log(\mu)$ cross sections of an entirely metastatic lymph node from a different patient. The color scales of Figs. 1 and 2 are the same for easier comparison. For this lymph node, the $\log(\mu)$ values were lower with a mean of –0.34 and a standard deviation of 0.22. The difference in the QUS voxel sizes between Figs. 1 and 2 is because of the change in overlap between adjacent

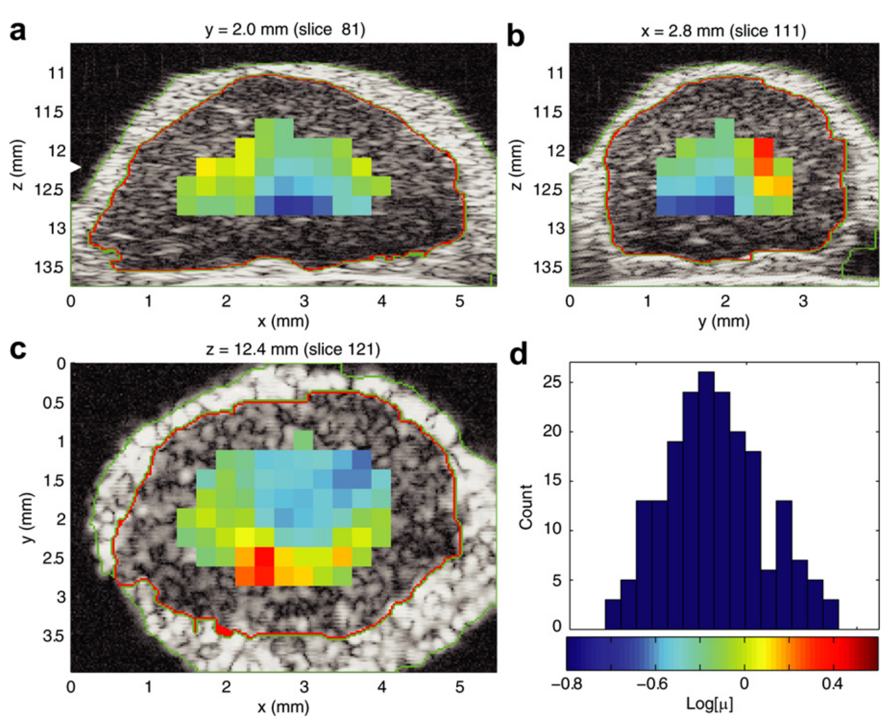

Fig. 1. (a–c) QUS cross-section images of $\log(\mu)$ of a non-metastatic lymph node. (d) Histogram of $\log(\mu)$ estimates. White arrows in (a) and (b) indicate the focal depth of the transducer.

ROIs depending on the total number of ultrasound voxels in the dataset. (See Table 1 in Mamou et al. 2010.)

The large variations in the estimates of $\log(\mu)$ shown in Figs. 1 and 2 illustrate how differentiating a metastatic node from a non-metastatic node potentially would be possible, but difficult using μ alone. The metastatic node globally has lower $\log(\mu)$ values and its QUS images are blue, whereas the QUS images of the non-metastatic node contain some yellow and red in addition to some blue.

Typical cross-section images of other QUS parameters have been published previously and, in particular, scatterer-size images demonstrated significant potential for diagnosis and cancer localization (Mamou et al. 2009b, 2009c, 2010).

Figures 3a and 3b displays the estimated PDFs from two ROIs located near the center of each of the lymph nodes displayed in Figs. 1 and 2. The Nakagami and HK fit obtained using our estimators are also shown. In the case of the HK model, our estimator only returns two (μ and k) of the three independent parameters of the HK model (eqn (4)). The third parameter, σ, was obtained from the second-order moment of the HK distribution (Hruska and Oelze 2009):

$$\sigma=\sqrt{\frac{E[R^2]}{k^2+2}}. \tag{10}$$

Examination of Figs. 3a and 3b indicates that the ROI PDFs are fitted better using the HK model because smaller root-mean-square errors (RMSEs) were obtained. In addition, these figures demonstrate that both estimated PDFs are not satisfactorily fit using the Nakagami model. Another interesting feature is that the values of the RMSEs from both models obtained in the case of the metastatic node (Fig. 3b) are more than twice those obtained in the case of the non-metastatic node (Fig. 3a).

Lymph node classification based on QUS estimates

For each lymph node, we averaged the eight QUS estimates over all of the ROIs that returned QUS estimates. The estimation algorithm was set to reject all QUS estimates from ROIs for which the scatterer size estimate was <5 μm. The algorithm also included a noise threshold to exclude ROIs for which the noise was judged to be too significant (Mamou et al. 2010). In the current study, more than 98% of all ROIs of all nodes returned QUS estimates and only six lymph nodes had ROIs in which the algorithm did not return estimates. Using the averaged estimates, we evaluated whether correctly classifying lymph nodes was possible based on these eight QUS estimates. Table 1 displays the average and standard

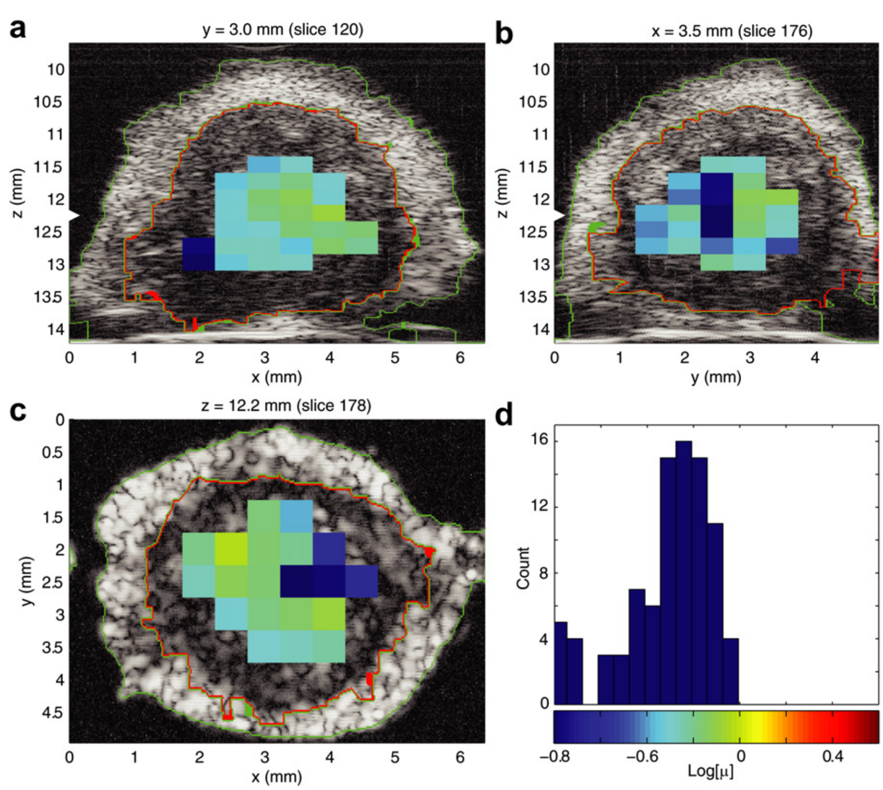

Fig. 2. (a–c) QUS cross-section images of $\log(\mu)$ of a completely metastatic lymph node. (d) Histogram of $\log(\mu)$ estimates. White arrows in (a) and (b) indicate the focal depth of the transducer.

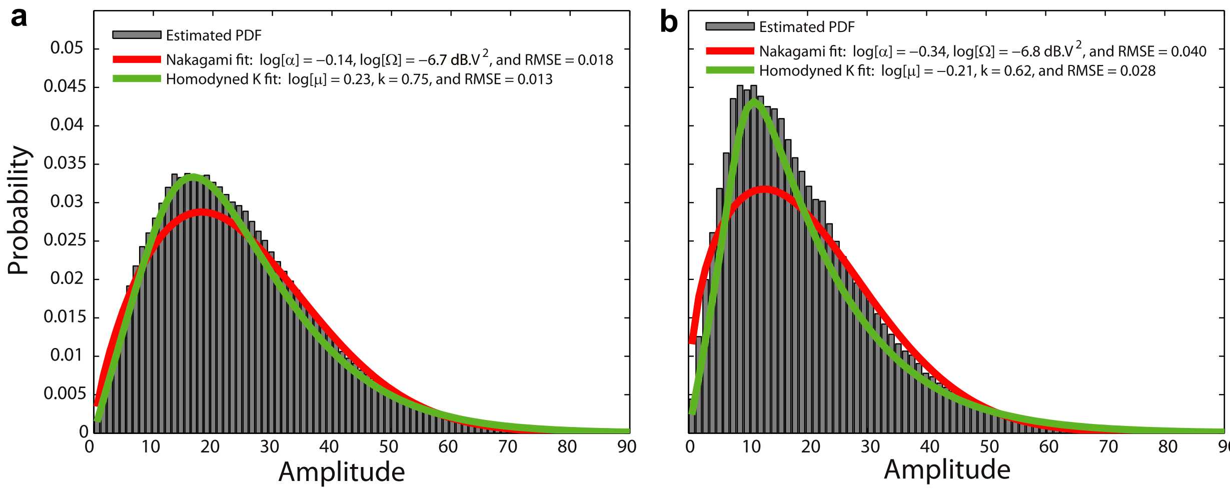

Fig. 3. (a, b) Estimated PDF and overlayed fits using the Nakagami and HK PDFs of an ROI near the center of the lymph nodes shown in Figs. 1 and 2, respectively.

deviations of the QUS estimates for the metastatic and non-metastatic nodes.

The statistics of the four QUS estimates based on backscatter spectral quantification are in strong agreement with our previously published results derived from a significantly lower number of lymph nodes (Mamou et al. 2010). The trend observed in Table 1 indicates that metastatic nodes have significantly larger effective scatterer-size estimates (*i.e.*, *D*), higher intercept estimates (*i.e.*, *I*) and significantly lower slope (*i.e.*, *S*) and acoustic-concentration estimates (*i.e.*, CQ^2). (Note that the analysis of variance [ANOVA] test showed statistical differences ($p < 0.05$) in metastatic and non-metastatic values for these four QUS parameters, which confirms results previously obtained with significantly fewer lymph nodes (Mamou et al. 2010).

The other four QUS estimates were obtained from the envelope statistics and the two distribution models (Table 1). No statistically significant differences were observed between the cancer-free and cancer-filled nodes for $\log(\Omega)$ and k, but estimates of $\log(\alpha)$ and $\log(\mu)$ were significantly lower in the metastatic lymph nodes. This is consistent with the physical interpretation of μ and α being related to scatterer number density. Metastatic nodes, which have larger effective scatterer-size estimates than non-metastatic nodes, are likely to have a concomitantly lower number density. Note that although statistically significant differences were observed for μ and α, the standard deviations of the estimates were fairly large and significant overlap existed between the estimates obtained between the two types of nodes. This also was illustrated in Figs. 1d and 2d for the μ parameter.

To visually illustrate the potential of the eight QUS estimates for classification, Fig. 4 displays the scatter plots of the QUS estimates obtained for the two different scattering models and the two different envelope-statistics models. Figure 4a shows good separation between the metastatic and non-metastatic nodes for size and concentration estimates. Some overlap exists in the range of sizes between 31 and 35 μm, but overall, the spherical Gaussian form-factor estimates show strong potential for detection of metastases. Similarly, Fig. 4b shows satisfactory separation, but more overlap is visible for S values between 0.05 and 0.22 dB/MHz. The other two panels show the results obtained by modeling envelope statistics with the Nakagami distribution (Fig. 4c) and the HK distribution (Fig. 4d). Overall, very poor separation is apparent; only a suggestion of smaller α and μ values is observed for metastatic nodes. This observation is consistent with the values reported in Table 1. Nevertheless, Fig. 4d reveals an interesting feature of the k estimates: every lymph node with an average value below 0.40 is non-metastatic and therefore,

Table 1. Average QUS estimates (means ± standard deviations) for non-metastatic and metastatic nodes

QUS estimate	Non-metastatic nodes ($N = 92$)	Metastatic nodes ($N = 20$)
D (μm)	28.6 ± 3.1*	36.7 ± 2.5*
CQ^2 (dB mm^{-3})	−3.73 ± 2.48*	−7.77 ± 4.31*
I (dB)	−63.1 ± 3.8*	−57.7 ± 4.7*
S (dB/MHz)	0.30 ± 0.11*	0.01 ± 0.11*
$\log(\alpha)$	−0.26 ± 0.05*	−0.32 ± 0.06*
$\log(\Omega)$(dB V^2)	−6.54 ± 0.22	−6.62 ± 0.39
$\log(\mu)$	−0.09 ± 0.19*	−0.35 ± 0.22*
k	0.56 ± 0.12	0.58 ± 0.10

* Statistical significance based on ANOVA results of $p < 0.05$.

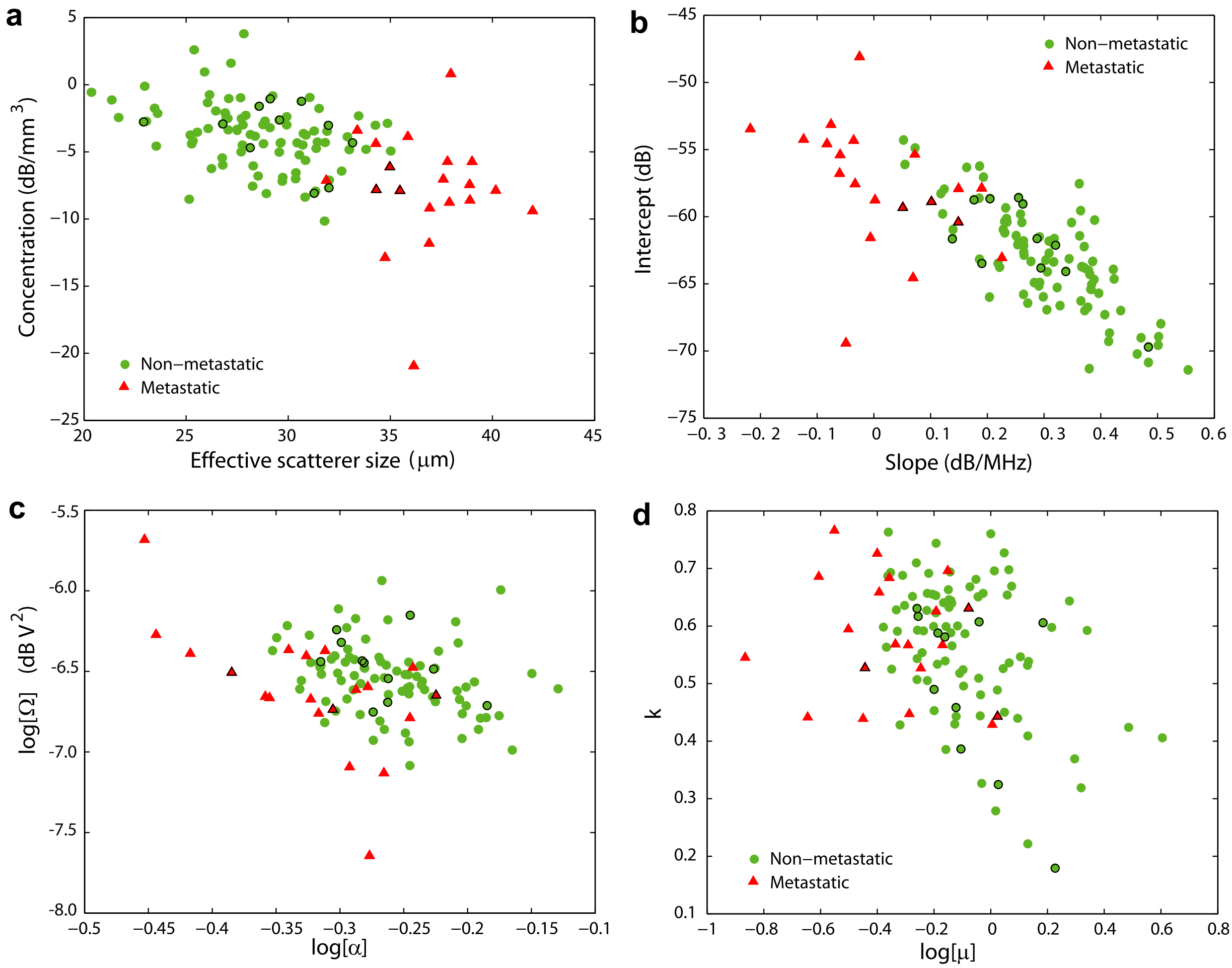

Fig. 4. Scatter plots of estimates by model. (a) Effective scatterer size and acoustic concentration (Gaussian form factor), (b) intercept and slope (straight-line model), (c) Nakagami envelope model and (d) homodyned-K envelope model. Gastric cancer nodes are outlined in black.

although the means of the k estimates are not statistically different (Table 1), the spread of the k estimates is larger for the non-metastatic nodes. This observation also indicates that nodes for which the incoherent signal is at least 2.5 times greater than the coherent signal are non-metastatic. In Fig. 4, the data points outlined in black denote the gastric cancer nodes. These scatter plots suggest that all QUS estimates obtained from gastric cancer nodes are very similar to those obtained from colorectal cancer nodes for metastatic and non-metastatic node types. (For both node types, the ANOVA test failed to find a statistical difference between gastric and colorectal nodes for any of the eight QUS estimates.)

To further quantify these observations, the software package SPSS (SPSS, Inc., Chicago, IL, USA) was used to generate receiver operating characteristic (ROC) curves for each individual QUS estimate and for several combinations of the eight QUS estimates using linear-discriminant analysis (Table 2). SPSS also was used to evaluate classification performance using a leave-one-out procedure and the resulting specificity, sensitivity and percentage of correctly classified nodes were computed (Table 2). Looking first at the numbers obtained with the four QUS estimates quantifying backscatter power spectra, the results indicate that by using D alone, nearly perfect classification performance can be achieved with an area under the ROC curve (AUC) of 0.986 $\pm$ 0.009. Specificity and sensitivity also were excellent, with both values above 91%. The moderate overlap among the acoustic concentration values (Fig. 4a) produced an AUC value of 0.829 $\pm$ 0.056, a specificity of 80% and a sensitivity of 70%; therefore, acoustic-concentration estimates alone would classify lymph nodes only moderately well. Combining D and CQ^2 only marginally improves classification performance over D alone (AUC value of 0.988). I alone performs moderately well and as well as CQ^2 alone, and S performs well with a performance only slightly

Table 2. Classification performance analysis of the ability of QUS estimates to discriminate between metastatic and non-metastatic nodes

QUS estimates	ROC AUC	95% CI	Sensitivity	Specificity	P_c
D	0.986 ± 0.009	0.969–1.000	95.0%	91.3%	92.0%
CQ^2	0.829 ± 0.056	0.719–0.939	70.0%	80.4%	78.6%
D and CQ^2	0.988 ± 0.009	0.971–1.000	95.0%	91.3%	92.0%
I	0.829 ± 0.058	0.716–0.942	75.0%	73.9%	74.1%
S	0.968 ± 0.016	0.936–0.999	90.0%	90.2%	90.2%
I and S	0.970 ± 0.015	0.940–1.000	90.0%	90.2%	90.2%
log(α)	0.768 ± 0.062	0.647–0.889	65.0%	70.7%	69.6%
log(Ω)	0.573 ± 0.077	0.422–0.724	60.0%	60.9%	60.7%
log(α) and log(Ω)	0.848 ± 0.053	0.743–0.952	70.0%	72.8%	72.3%
k	0.526 ± 0.072	0.384–0.667	55.0%	55.4%	55.4%
log(μ)	0.815 ± 0.058	0.702–0.929	70.0%	73.9%	73.2%
k and log(μ)	0.815 ± 0.058	0.702–0.929	70.0%	73.9%	73.2%
D and k	0.996 ± 0.003	0.989–1.000	95.0%	95.7%	95.5%

Areas under the ROC curve (AUC) include the standard errors in the area estimates. Sensitivity, specificity and the percentage of correctly classified nodes (P_c) were obtained using linear discriminant analysis with a leave-one-out procedure.

inferior to D alone. Finally, combining I and S together produces an AUC value of 0.970 ± 0.015, with sensitivity and specificity values of 90%.

Results for the other four QUS estimates based on envelope statistics indicate that diagnostic performance using any of these estimates alone would be unsatisfactory. AUC values obtained from Ω or k were smaller than 0.6. The Nakagami parameter, α, performed significantly better, but it still produced a mediocre AUC value of 0.768. Finally, the best performance was obtained using μ, leading to an AUC value of 0.815 with sensitivity and specificity values >70%. Interestingly, combining the Nakagami model parameters, α and Ω, led to an AUC value of 0.848, meaning that the Nakagami envelope model would classify lymph nodes moderately well. However, combining the two HK model parameters, k and μ, did not improve classification performance over μ alone. Nevertheless, the HK and Nakagami model classification performance only remains moderately satisfactory. These results indicate that the HK model produced the best QUS estimate (*i.e.*, μ) for classification based on envelope quantification, but they also indicate that the Nakagami model slightly outperformed the HK model when the two independent QUS estimates from each model were combined.

Interestingly, the best classification results were obtained by combining D and k, which led to an AUC value of 0.996 ± 0.003 and sensitivity and specificity values of 95%. (No other combination of two or more QUS estimates led to a better performance.) Figure 5 shows the scatter plot of these two parameters and indicates that the separation between the cancer-containing and cancer-free nodes is better than on any of the other scatter plots shown in Fig. 4. Although the mean and standard deviation of k between each node type were essentially the same (Table 1), this parameter was able to improve classification performance over D alone. To investigate this fact, we looked at the distribution of k values among the nodes that had D estimates between 28.4 and 37.0 μm. This range of sizes was obtained by considering the mean of the two average values of D for each node class (*i.e.*, 32.7 μm) and adding or removing the ensemble standard deviation of D (*i.e.*, 4.3 μm). This procedure led to the selection of 60 nodes (49 non-metastatic nodes and 11 metastatic nodes) that had overlapping values of D for non-metastatic and metastatic nodes. The average k estimates within this selection were found to be 0.61 ± 0.11 and 0.53 ± 0.12 for metastatic and non-metastatic nodes, respectively. In addition, the ANOVA test returned a p-value of 0.067 for these k estimates. These numbers indicate that in the region where a classifier based on D alone would be most likely to make classification errors, k estimates tend to be different for non-metastatic and

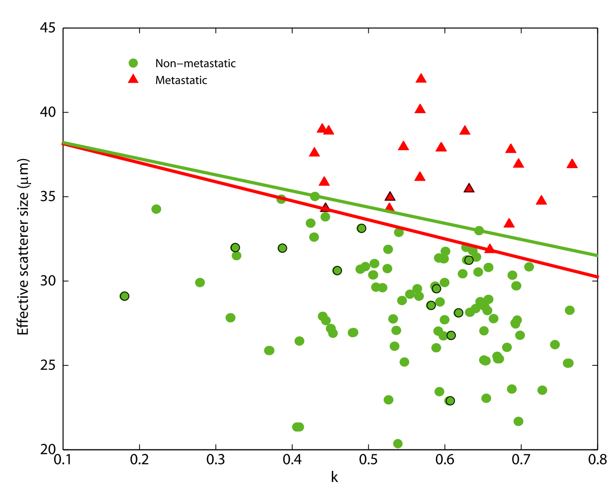

Fig. 5. Scatter plot of best estimate combination for classification (k and D) and illustration of possible classification performance at 100% specificity (*green solid line*) or 100% sensitivity (*red solid line*). Gastric cancer nodes are outlined in black.

metastatic nodes, and can positively influence classification performance; this is consistent with Table 2 and Fig. 5.

Additionally, Fig. 5 illustrates how a 100%-specificity or a 100%-sensitivity classifier could be designed using a linear combination of k and D. The green solid line passes through the two non-metastatic lymph nodes that are the closest to the mean of all the metastatic nodes; therefore, if this line is established as a classifier threshold and all nodes above the line are declared to be metastatic and all nodes below the line to be non-metastatic, then 100% specificity will be achieved with a sensitivity of 90%. Similarly, the red solid line would lead to a classifier with 100% sensitivity (all metastatic nodes are classified correctly) at a specificity of 97.5%. Clinically, the 100% sensitivity approach is more relevant; it guarantees that no cancer will be missed and potentially could significantly reduce the number of nodes requiring histological evaluation by reliably identifying cancer-free nodes and, more important, could identify suspicious regions for detailed histological evaluation that contain small metastases that would be overlooked using standard histology procedures. Here, instead of 112 nodes, only 22 would be sent to histology and no cancer would be overlooked. These methods would serve as an adjunct to histopathology that would improve the efficiency of histological procedures for node evaluations.

In summary, Tables 1 and 2 and Figs. 4 and 5 present very satisfactory results. Our QUS methods are able to classify the nodes that either are completely metastatic or are completely free of metastatic tissue nearly perfectly using only one (D) or two QUS estimates (D and k). Finally, based on the current results, the spherical Gaussian scattering model slightly outperforms the straight-line model. In addition, the results indicate that of the four QUS estimates from the two proposed envelope models, the μ parameter obtained from the more advanced HK model provides the best classification performance.

DISCUSSION

The studies presented herein initially were motivated by earlier studies performed at lower frequencies (*i.e.*, 10 MHz) that suggested spectral intercept estimates produced a very high AUC value for lymph node classification (Feleppa et al. 1997). More recent studies performed at higher frequencies on 46 lymph nodes resulted in perfect classification using D or S alone (Mamou et al. 2010). Subsequently, we significantly extended these studies by investigating 112 lymph nodes, and also quantifying envelope statistics using a commonly used classic model (*i.e.*, Nakagami) and a more involved model (HK) using an efficient and robust algorithm (Hruska and Oelze 2009).

Estimating the four QUS envelope parameters using a maximum-likelihood estimator for α and Ω and the fractional-order moment algorithm for μ and k increased computation time by only 15% when compared with estimating only the four other QUS estimates; however, computation times remained far from real time. To obtain the eight QUS estimates for an entire lymph node required an average time of 20 minutes. In their present form, all of the algorithms were implemented in MATLAB (The MathWorks Inc., Natick, MA, USA) because of its convenience for research-oriented signal and image processing. Nevertheless, this time frame is amenable to intraoperative characterization. (Conventional histology usually takes at least one day to provide diagnostic results.) Eventually, the final algorithms will be converted and compiled as efficient executables using C++. In addition, once we have isolated the best QUS estimates for classification, only those would need to be computed. For example, based on the results to date and presented in Table 2, only k and D would need to be estimated. A decrease in computation time of about 30% was observed when only estimates of k and D were computed for an entire lymph node using MATLAB.

The 3-D QUS methods presented in this study permitted virtually perfect classification of a relevant number of lymph nodes that either were nearly completely metastatic or were entirely non-metastatic. Therefore, in the future, we will apply and evaluate these methods in studies of lymph nodes with smaller micrometastatic foci that do not fill the node. The hypothesis we will test in partially metastatic lymph nodes is that 3-D QUS estimates can reliably detect small cancer-containing regions including clinically significant micrometastasis. Because we also have the 3-D histology data with histologically defined cancer regions, we will easily be able to evaluate the performance of the QUS methods. In particular, an important question would be to determine the smallest size of metastatic foci that we can detect. To detect clinically relevant micrometastases (*i.e.*, diameter between 0.2 and 2 mm), we may need to decrease the size of the ROIs to improve the QUS-image spatial resolution. Based on empirical published criteria, using cylindrical ROIs with a diameter of 0.6 mm and a length of 0.4 mm with our imaging system should not increase bias or variance of QUS estimates quantifying backscatter significantly (Oelze and O'Brien 2004a), but such ROIs would significantly improve 3-D QUS image resolution. Further resolution improvements also may be possible using methods that correct for ROIs with suboptimal lengths (Oelze and O'Brien 2004b). In addition, another option would be to use an ultrasound transducer with a higher center frequency, which would allow smaller ROIs;

however, the trade-off would be the decreased penetration depth of the higher-frequency ultrasound and therefore a reduced ability to obtain QUS estimates deep into lymph nodes.

In this study, the same ROIs used for the spectral estimates were used to produce the envelope statistics. Envelope statistics are notorious for large variances if the sample size (*i.e.*, the size of the ROI) is too small. In the future, the variances of the envelope statistics could be reduced with larger ROIs. Regions of suspicion within a node could be determined based on estimates of effective scatterer size. Within the suspicious regions, larger ROIs could be selected to produce envelope-statistics estimates with smaller variances. Envelope statistics would produce images with poorer spatial resolution, but with improved classification resulting from a reduction in the variance of the estimates.

Finally, we have initiated analyses of RF data from axillary lymph nodes, including sentinel nodes, of breast cancer patients based on what we have learned from the more available and architecturally simpler abdominal nodes of colorectal and gastric cancer patients. Axillary nodes present complications associated with intranodal inclusions, which appear to be small, fatty deposits. Therefore, our approach must be modified to exclude these fatty regions from QUS processing. To achieve this goal, efforts are being directed toward improving the 3-D segmentation methods to isolate these regions even though they are surrounded by nodal tissue.

Acknowledgments—Supported in part by NIH Grant CA100183. The authors thank Helena Herman and Justin Rhoda for their help with the 3-D segmentation of the lymph nodes.

REFERENCES

Aristizábal O, Christopher DA, Foster FS, Turnbull DH. 40-MHz echocardiography scanner for cardiovascular assessment of mouse embryos. Ultrasound Med Biol 1998;24:1407–1417.

Baddour RE, Sherar MD, Hunt JW, Czarnota GJ, Kolios MC. High-frequency ultrasound scattering from microspheres and single cells. J Acoust Soc Am 2005;117:934–943.

Coron A, Mamou J, Hata M, Machi J, Yanagihara E, Laugier P, Feleppa EJ. Three-dimensional segmentation of high-frequency ultrasound echo signals from dissected lymph nodes. Proceedings of the 2008 IEEE Ultrasonics Symposium 2008:1370–1373.

de Korte CL, van der Steen AF, Céspedes EI, Pasterkamp G, Carlier SG, Mastik F, Schoneveld AH, Serruys PW, Bom N. Characterization of plaque components and vulnerability with intravascular ultrasound elastography. Phys Med Biol 2000;45:1465–1475.

Destrempes F, Cloutier G. A critical review and uniformized representation of statistical distributions modeling the ultrasound echo envelope. Ultrasound Med Biol 2010;36:1037–1051.

Dutt V, Greenleaf JF. Ultrasound echo envelope analysis using a homodyned K distribution signal model. Ultrason Imaging 1994;16: 265–287.

Dutt V, Greenleaf JF. Speckle analysis using signal to noise ratios based on fractional order moments. Ultrason Imaging 1995;17:251–268.

Eltoft T. The Rician inverse Gaussian distribution: A new model for non-Rayleigh signal amplitude statistics. IEEE Trans Image Proc 2005; 14:1722–1735.

Feleppa EJ, Lizzi FL, Coleman DJ, Yaremko MM. Diagnostics spectrum analysis in ophthalmology: A physical perspective. Ultrasound Med Biol 1986;12:623–631.

Feleppa EJ, Machi J, Noritomi T, Tateishi T, Oishi R, Yanagihara E, Jucha J. Differentiation of metastatic from benign lymph nodes by spectrum analysis in vitro. Proceedings of the 1997 IEEE Ultrasonics Symposium 1997:1137–1140.

Hao X, Bruce CJ, Pislaru C, Greenleaf JF. Characterization of reperfused infarcted myocardium from high-frequency intracardiac ultrasound imaging using homodyned K distribution. IEEE Trans Ultrason Ferroelectr Freq Control 2002;49:1530–1542.

Hruska DP. Improved techniques for statistical analysis of the envelope of backscattered ultrasound using the homodyned K distribution. M.S. thesis. University of Illinois at Urbana-Champaign, 2009.

Hruska DP, Oelze ML. Improved parameter estimates based on the homodyned K distribution. IEEE Trans Ultrason Ferroelectr Freq Control 2009;56:2471–2481.

Hruska DP, Sanchez J, Oelze ML. Improved diagnostics through quantitative ultrasound imaging. Proceedings of the Annual International Conference of the IEEE Engineering in Medicine and Biology Society EMBC 2009:1956–1959.

Huang YP, Zheng YP, Leung SF, Choi AP. High frequency ultrasound assessment of skin fibrosis: Clinical results. Ultrasound Med Biol 2007;33:1191–1198.

Insana MF, Wagner RF, Brown DG, Hall TJ. Describing small-scale structure in random media using pulse-echo ultrasound. J Acoust Soc Am 1990;87:179–192.

Jakeman E. On the statistics of K-distributed noise. J Phys A Math Gen 1980;13:31–48.

Kino GS. Acoustic waves. Englewoods Cliffs, NJ: Prentice Hall; 1987.

Kolios MC, Czarnota GJ, Lee M, Hunt JW, Sherar MD. Ultrasonic spectral parameter characterization of apoptosis. Ultrasound Med Biol 2002;28:589–597.

Lizzi FL, Greenebaum M, Feleppa EJ, Elbaum M, Coleman DJ. Theoretical framework for spectrum analysis in ultrasonic tissue characterization. J Acoust Soc Am 1983;73:1366–1373.

Mamou J, Aristizábal O, Silverman RH, Ketterling JA, Turnbull DH. High-frequency chirp ultrasound imaging with an annular array for ophthalmologic and small-animal imaging. Ultrasound Med Biol 2009a;35:1198–1208.

Mamou J, Coron A, Hata M, Machi J, Yanagihara E, Laugier P, Feleppa EJ. High-frequency quantitative ultrasound imaging of cancerous lymph nodes. Japan J Appl Phys 2009b;48. 07GK08–1–8.

Mamou J, Coron A, Hata M, Machi J, Yanagihara E, Laugier P, Feleppa EJ. Three-dimensional high-frequency characterization of excised human lymph nodes. Proceedings of the 2009 IEEE Ultrasonics Symposium 2009c:45–48.

Mamou J, Coron A, Hata M, Machi J, Yanagihara E, Laugier P, Feleppa EJ. Three-dimensional high-frequency characterization of cancerous lymph nodes. Ultrasound Med Biol 2010;36:361–375.

Mamou J, Oelze ML, O'Brien WD Jr, Zachary JF. Extended three-dimensional impedance map methods for identifying ultrasonic scattering sites. J Acoust Soc Am 2008;123:1195–1208.

Martin-Fernandez M, Cardenes R, Alberola-Lopez C. Parameter estimation of the homodyned K distribution based on signal to noise ratio. IEEE International Ultrasonics Symposium, New York, 2007:158–161.

Mills SE. Histology for pathologists. 3rd ed. Philadelphia: Lippincott Williams & Wilkins; 2006.

Nakagami M. The m-distribution-A general formula of intensity distribution in rapid fading. In: Statistical methods on wave propagation. New York: Pergamon Press; 1960. p. 3–36.

Oelze ML, O'Brien WD Jr. Defining optimal axial and lateral resolution for estimating scatterer properties from volumes using ultrasound backscatter. J Acoust Soc Am 2004a;115:3226–3234.

Oelze ML, O'Brien WD Jr. Improved scatterer property estimates from ultrasound backscatter for small gate lengths using a gate-edge correction factor. J Acoust Soc Am 2004b;116:3212–3223.

Oelze ML, Zachary JF. Examination of cancer in mouse models using high-frequency quantitative ultrasound. Ultrasound Med Biol 2006;32:1639–1648.

Oelze ML, Zachary JF, O'Brien WD Jr. Characterization of tissue microstructure using ultrasonic backscatter: Theory and technique for optimization using a Gaussian form factor. J Acoust Soc Am 2002;112:1202–1211.

Ossant F, Patat F, Lebertre M, Teriierooiterai ML, Pourcelot L. Effective density estimators based on the K distribution: Interest of low and fractional order moments. Ultrason Imaging 1998;20:243–259.

Prager RW, Gee AH, Treece GM, Berman LH. Analysis of speckle in ultrasound images using fractional order statistics and the homodyned K distribution. Ultrasonics 2002;40:133–137.

Raju BI, Srinivasan MA. Statistics of envelope of high-frequency ultrasonic backscatter from human skin in vivo. IEEE Trans Ultrason Ferroelectr Freq Control 2002;49:871–882.

Saijo Y, Tanaka A, Owada N, Akino Y, Nitta S. Tissue velocity imaging of coronary artery by rotating-type intravascular ultrasound. Ultrasonics 2004;42:753–757.

Shankar PM. A model for ultrasonic scattering from tissues based on the K distribution. Phys Med Biol 1995;40:1633–1649.

Shankar PM. A general statistical model for ultrasonic backscattering from tissues. IEEE Trans Ultrason Ferroelectr Freq Control 2000; 47:727–736.

Shankar PM, Dumane VA, Reid JM, Genis V, Forsberg F, Piccoli CW, Goldberg BB. Use of the K-distribution for classification of breast masses. Ultrasound Med Biol 2000;26:1503–1510.

Shankar PM, Dumane VA, Reid JM, Genis V, Forsberg F, Piccoli CW, Goldberg BB. Classification of ultrasonic B-mode images of breast masses using Nakagami distribution. IEEE Trans Ultrason Ferroelectr Freq Control 2001;48:569–580.

Silverman RH, Ketterling JA, Mamou J, Coleman DJ. Improved high-resolution ultrasonic imaging of the eye. Arch Ophthalmol 2008; 126:94–97.

Silverman RH, Rondeau MJ, Lizzi FL, Coleman DJ. Three-dimensional high-frequency ultrasonic parameter imaging of anterior segment pathology. Ophthalmology 1995;102:837–843.

Tsui PH, Chang CC. Imaging local scatterer concentrations by the Nakagami statistical model. Ultrasound Med Biol 2007;33: 608–619.

Tsui PH, Yeh CK, Liao YY, Chang CC, Kuo WH, Chang KJ, Chen CN. Ultrasonic Nakagami imaging: A strategy to visualize the scatterer properties of benign and malignant breast tumors. Ultrasound Med Biol 2010;36:209–217.

Tunis AS, Czarnota GJ, Giles A, Sherar MD, Hunt JW, Kolios MC. Monitoring structural changes in cells with high-frequency ultrasound signal statistics. Ultrasound Med Biol 2005;31:1041–1049.

Turnbull DH. Ultrasound backscatter microscopy of mouse embryos. Methods Mol Biol 2000;135:235–243.

Turnbull DH, Foster FS. Ultrasound biomicroscopy in developmental biology. Trends Biotechnol 2002;20:S29–S33.

van der Valk P, Meijer CJ. The histology of reactive lymph nodes. Am J Surg Pathol 1987;11:866–882.

Vogt M, Ermert H. In vivo ultrasound biomicroscopy of skin: Spectral system characteristics and inverse filtering optimization. IEEE Trans Ultrason Ferroelectr Freq Control 2007;54:1551–1559.

Wagner RF, Insana MF, Brown DG. Statistical properties of radio-frequency and envelope-detected signals with applications to medical ultrasound. J Opt Soc Am A 1987;4:910–922.